Jeff R. Harris
Department of Mechanical and
Aerospace Engineering,
Utah State University,
Logan, UT 84322
e-mail: jeff.harr@aggiemail.usu.edu

Blake W. Lance
Department of Mechanical and
Aerospace Engineering,
Utah State University,
Logan, UT 84322
e-mail: b.lance@aggiemail.usu.edu

Barton L. Smith
Professor
Fellow ASME
Department of Mechanical and
Aerospace Engineering,
Utah State University,
Logan, UT 84322
e-mail: barton.smith@usu.edu

Experimental Validation Data for Computational Fluid Dynamics of Forced Convection on a Vertical Flat Plate

A computational fluid dynamics (CFD) validation dataset for turbulent forced convection on a vertical plate is presented. The design of the apparatus is based on recent validation literature and provides a means to simultaneously measure boundary conditions (BCs) and system response quantities (SRQs). All important inflow quantities for Reynolds-Averaged Navier-Stokes (RANS). CFD are also measured. Data are acquired at two heating conditions and cover the range $40{,}000 < Re_x < 300{,}000$, $357 < Re_{\delta_2} < 813$, *and* $0.02 < Gr/Re^2 < 0.232$. [DOI: 10.1115/1.4031007]

1 Introduction

The primary purpose of this work is to generate and disseminate experimental data for CFD validation for forced convection on a vertical plate. In addition, some features and differences of buoyancy aided and opposed forced convection will be discussed.

This facility, instrumentation, and measurements are described in detail. The SRQs include the heat flux from the plate at three locations and the velocity field over the heated plate (including wall shear stress) at the same three locations. All inputs required for the numerical model, including BCs, inflow velocity, and temperature and material properties are measured. All SRQs, BCs, and inflow data may be accessed using data in the supplemental results which are available under "Supplemental Data" tab for this paper on the ASME Digital Collection. The data and descriptions required to satisfy the completeness level (as outlined in Ref. [1]) for the validation data are also provided along with some description included in this document and in the Supplemental results which are available under "Supplemental Data" tab for this paper on the ASME Digital Collection.

Obtaining validation data from journal articles is inconvenient. Online databases are better suited for dissemination of validation data and documentation of the experiment. Though some validation datasets are available from online databases, these typically lack the detail necessary to fully describe the measurements and uncertainties [1]. Many such sources are listed at the CFD-Online website [2], including the National Aeronautics and Space Administration (NASA) NPARC Alliance Verification and Validation Archive [3] and the European Research Community on Flow, Turbulence and Combustion database [4]. As part of the present effort, a database was developed to enable users to download the BCs, SRQ data, and other relevant information to conduct their own validation studies, using the same BCs to which the SRQ data correspond [5]. This database is included in the Supplemental results which are available under "Supplemental Data" tab for this paper on the ASME Digital Collection.

1.1 Model Validation.

Validation is "the process of determining the degree to which a model is an accurate representation of the real world from the perspective of the intended uses of the model" [6,7]. To perform a CFD validation study, one must have measurements of both the model inputs and outputs.

The model outputs, or SRQs, are the quantities to be compared between the experiment and the simulation. No specific application motivates the present work, and we seek to produce the most broadly useful dataset possible. To this end, we consider the recommendations of Oberkampf and Roy [6], who described the difficulty spectrum of measurements and computed quantities, as shown in Fig. 1. Using SRQs from a wide range of the spectrum will ensure a more robust validation study. For instance, the model that best predicts boundary layer velocity for this particular experiment (dependent variable) may not predict the heat flux (derivative of a dependent variable) as accurately. Using SRQs from a wide range on the spectrum will better determine which model is the best predictor of the physical phenomena. In the present study, SRQs are chosen based on project budget and time constraints while covering as much of the spectrum as possible.

Many have recommended (e.g., Ref. [6]) that model validation be performed in a hierarchy, as shown in Fig. 2, with the lower tiers involving simpler physics and higher resolution measurement and the top tier covering the complete system of interest with more coarse measurements. Since the heat transfer and the fluid flow are coupled, this problem cannot be considered as a unit problem. To meet the requirements of the benchmark tier in the

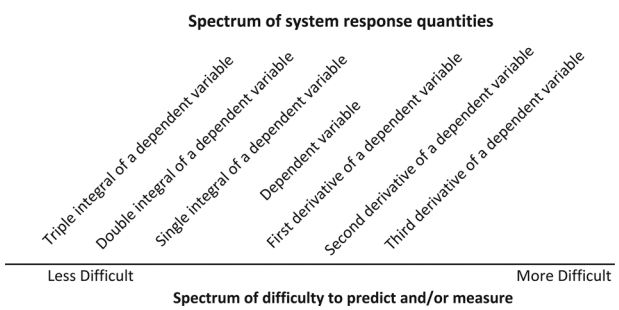

Fig. 1 The difficulty spectrum of SRQs, after Ref. [6]

Contributed by the Fluids Engineering Division of ASME for publication in the JOURNAL OF FLUIDS ENGINEERING. Manuscript received April 15, 2014; final manuscript received July 4, 2015; published online August 10, 2015. Editor: Malcolm J. Andrews.

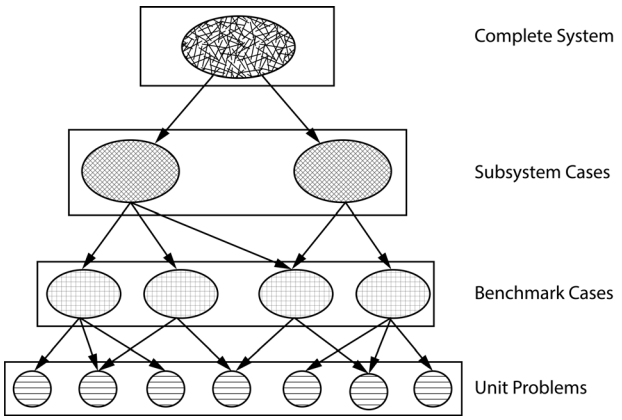

Fig. 2 The validation hierarchy with cross-hatch showing the amount of detail in each level, after Ref. [6]

validation hierarchy, the hardware used in this wind tunnel was specially fabricated to validate specific aspects of flow over a heated flat plate. The experiments were carried out in a new facility made specifically for benchmark tier validation experiments. The wind tunnel and plate are the simplified hardware meant to improve predictive capability of complicated flow physics for real-world scenarios for many applications. The inputs required to perform a CFD simulation (wall locations and temperatures, as well as inlet temperature and velocity) were measured and their uncertainties were estimated.

Figure 3 is used to illustrate the importance of using measured inflow conditions in a simulation. It is a common practice in CFD simulations to assume an idealized inlet profile, such as a parabolic or uniform profile. For our wind tunnel, a uniform inlet velocity assumption is valid for most of the inlet area, but not in the boundary layer. It is also a common practice to assume that the Reynolds normal stress at the inlet is a fixed percentage of the time-mean velocity (10% of the free stream velocity in this example), while the measured turbulence level is found to be large only in the thin boundary layers near the walls.

It is necessary to know the uncertainty of the experimental data as well as the simulation uncertainty to obtain the model uncertainty [6,8]. Therefore, the SRQ data must have quantified uncertainty. Since the simulation uses experimentally determined

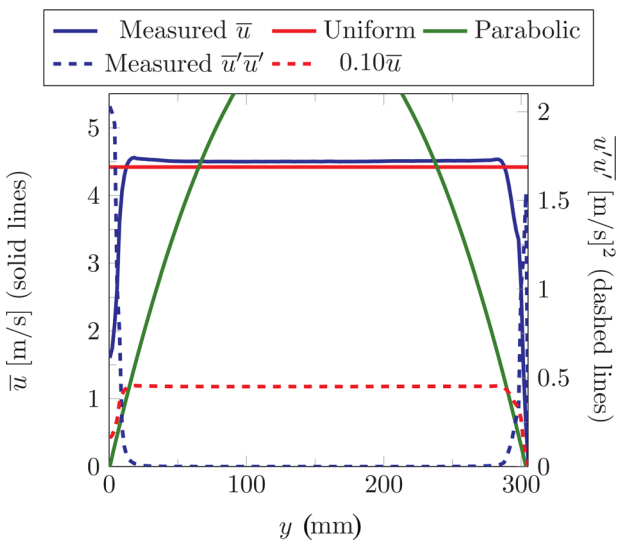

Fig. 3 A velocity profile for the inlet of the test section is shown, along with uniform and parabolic profiles. The Reynolds stress is also plotted along with a line of 10% of the time-mean streamwise velocity.

BCs, uncertainty is introduced into the simulation from uncertainty in the measurements. This also necessitates the uncertainty quantification of measured BCs.

Both inflow and SRQs for the present study are velocity data measured with particle image velocimetry (PIV). The uncertainty of the velocity measurements is quantified using the methods described by Timmins et al. [9], Warner et al. [10], and Wilson and Smith [11,12]. Other measured BCs include the wall geometry and temperature and inlet air temperature. The uncertainties of these quantities are determined using methods discussed by Coleman and Steele [13]. The manufacturer provided the uncertainty of the heat flux sensors used in this study. The uncertainty of wall locations, wall shear stress, and other quantities is discussed below.

1.2 Forced Convection. The forced convection regime theoretically has little effect from gravity (buoyancy) and is defined as $\mathrm{Gr}_x/\mathrm{Re}_x^2 < 0.3$ [14], where the local Grashof number is $g\beta(T_s - T_\infty)x^3/\nu^2$ and the local Reynolds number is $\bar{u}_\infty x/\nu$, with the inlet velocity $\bar{u}_\infty = 4.48$ m/s. For the purpose of this study, the kinematic viscosity ν is determined from the measured atmospheric air properties. Lloyd and Sparrow [15] conducted a theoretical analysis of forced convection over an isothermal vertical surface and cited experimental data for the same flow scenario. A later experimental study of convection from a vertical heated plate was presented by Gryzagoridis [16], who used hot-wire anemometry to measure the flow velocity. Temperature profiles were used to find heat transfer rates. These measurements, though state-of-the-art at the time, were obtrusive and therefore less useful for CFD validation.

Wang et al. [17] presented an experimental study of a heated vertical plate similar to the one considered in this work. The velocity was measured using a two-component laser Doppler anemometry system, which is unobtrusive, but provides a point velocity rather than a velocity field. Temperature measurements were acquired using a thermocouple rake and a correlation was presented for $\mathrm{Nu}_x = hx/k$, which can be used to understand the effects of buoyancy on heat transfer. While the study provided much useful insight, it was not intended for CFD validation. The necessary BCs were not reported nor were the measurement uncertainties.

Finally, a study that used PIV to study the velocity field along a heated plate was described by Hattori et al. [18]. The measurements were also acquired using hot-wire anemometry. The study focused on the laminarization of the flow and provided valuable information using PIV measurements for convection flow from a vertical plate. Again, the measurements obtained were not intended for CFD validation and are incomplete for that purpose.

This is a small sample of published studies on forced convection. A large number of studies show that forced convection is a mature field. However, each of these studies was a discovery experiment rather than a validation data experiment. The present study represents the first validation data study for forced convection known to the authors.

In what follows, we will describe our facility and measurements followed by a description of the data acquisition procedures. This will be followed by the BCs and SRQ results of two nominally isothermal cases: (1) buoyancy-aided forced convection and (2) buoyancy-opposed forced convection. Several comparisons will be presented showing the small but detectable effects on the flow due to the gravitational direction.

2 Facility and Measurements

2.1 Rotatable Buoyancy Tunnel. The experimental apparatus used for this project is called the rotatable buoyancy wind tunnel (RoBuT). The $12 \times 12 \times 78$ in. ($305 \times 305 \times 1981$ mm) test section is fixed to a Ferris wheel-like frame that allows the direction of gravity relative to the flow to be changed without

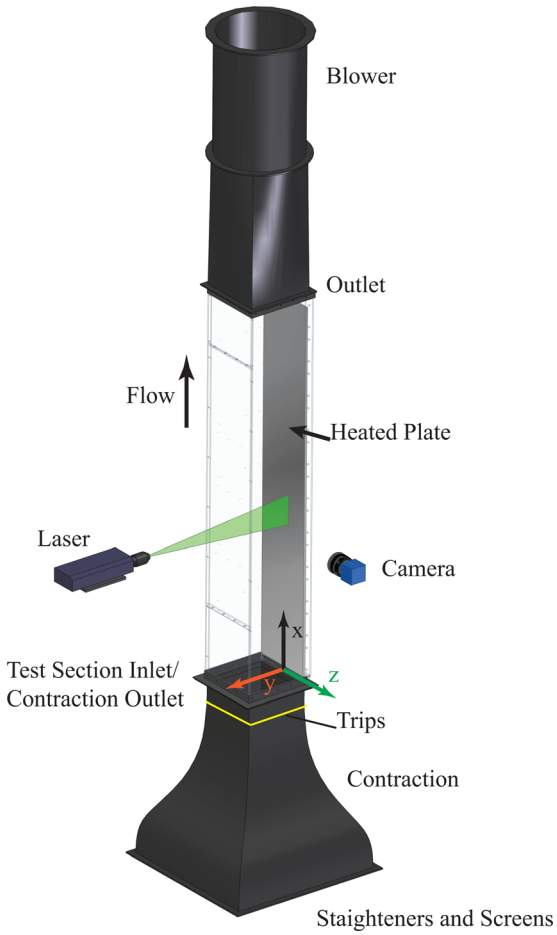

Fig. 4 A schematic of the wind tunnel showing the inlet contraction, test section, and the coordinate system

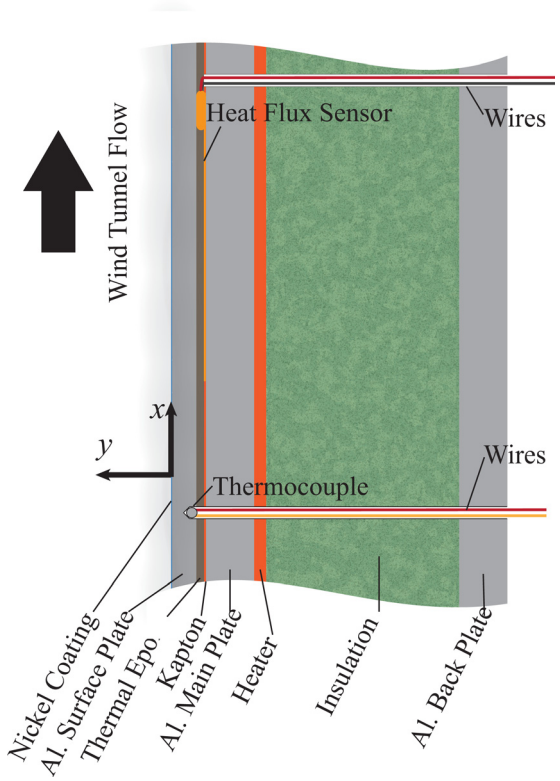

Fig. 5 Cross section of the heated wall

modifying the wind tunnel inlet or test section. Figure 4 shows a schematic of the RoBuT without its rotating frame.

This facility is intended for benchmark level validation where two or more different physical phenomena (such as momentum and heat transfer) are analyzed [6]. A benchmark tier validation experiment uses special hardware meant to represent main features of subsystems. The square test section allows for easy characterization of the inflow using planar PIV. Simultaneous measurements of BCs (wall temperature, inlet temperature, and atmospheric properties) and SRQs (boundary layer velocity and heat flux) can be acquired. PIV is used to measure all of the velocity data (both at the inlet and for SRQs). For additional details on the facility, see Supplemental results which are available under "Supplemental Data 26" tab for this paper on the ASME Digital Collection.

2.1.1 Test Section. The test section is made of three optically clear Lexan® walls that are 12.7 mm (0.5 in.) thick. The walls are referenced using the coordinate system in Fig. 4, where the heated plate is at $y = 0$ with $x = 12.7$ mm (0.5 in.) being the leading edge of the heated plate, and the left and right walls are at $z = -152.4$ mm (-6 in.) and $z = 152.4$ mm (6 in.), respectively. The wall opposite the heated plate is at $y = 304.8$ mm (12 in.) and is also referred to as the top wall.

The fourth wall is formed by the heated plate and its mounting components. A cross section of the plate near one of the heat flux sensors is shown in Fig. 5. The exterior wall of the tunnel is formed by an aluminum back plate. A layer of insulation lies between the back plate and an electric heater, which is pressed against a second aluminum plate on its other side. The heat flux sensor is potted between two aluminum plates with thermal epoxy and surrounded with Kapton, which has a similar thermal resistance. The aluminum surface plate is nickel coated on the air side to suppress radiation. For additional information about the heated plate, see Supplemental results which are available under "Supplemental Data 28" tab for this paper on the ASME Digital Collection.

Two methods are used to estimate the emissivity of the nickel-coated plate. First, from Howell et al. [19], the normal emissivity is

$$\varepsilon_n = \frac{4n}{(n+1)^2 + k_r^2} \tag{1}$$

where $n = 5.76$ and $k_r = 27.34$ are material constants for nickel-plated aluminum at 413 K ($\lambda = 7.0\,\mu$m to find the optical properties n and k in Ref. [19]). Equation (1) gives a normal emissivity of 0.029.

Second, the plate emissivity can be estimated by performing an energy balance on the surface of the nickel plate

$$q'' = h(T_s - T_\infty) + \varepsilon_n \sigma T_s^4 - \varepsilon_L \sigma T_L^4 \tag{2}$$

The emissivity of the Lexan ε_L is assumed to be 0.9. Using measured data from a natural convection state, the emissivity of the heated plate is estimated to be 0.034, which is in good agreement with Eq. (1). A Taylor series method uncertainty propagation [13] is used to compute the uncertainty of the plate emissivity using the energy balance method and is found to be on the order of the computed emissivity itself.

The heated plate is surrounded on the leading, trailing, and spanwise edges with blocks of Teflon® to allow for thermal expansion and to increase the thermal resistance between the heated plate and the Lexan side walls. Springs and a silicone rubber gasket at the outlet of the test section push the plate assembly toward the inlet, minimizing gaps. A layer of insulation on the outer side of the heaters (the right of Fig. 5) increases heat flux

from the plate into the test section. The insulation only serves to increase the efficiency of the heaters, ensuring that most of the power from the heaters goes into the flow. For analysis of the heat flow through the layers of the plate, see Supplemental results which are available under "Supplemental Data 1" tab for this paper on the ASME Digital Collection. Note that the heat flux was measured using sensors, not heater power. All the other materials are described in the Supplemental results which are available under "Supplemental Data" tab for this paper on the ASME Digital Collection.

2.1.2 Inflow. The inlet to the wind tunnel includes a contraction with a 6.25:1 area reduction. The inlet to the contraction includes honeycomb flow straighteners and screens (see Fig. 4). A 3.175 mm (1/8 in.) square trip is fixed to each of the four walls at a position 11.6 cm (4.58 in.) upstream of the heated plate leading edge. These trips make the transition location consistent between datasets.

The test section inlet velocity time-mean, kinetic energy, and dissipation are derived from the experimental inlet measurements acquired at $x = 0$. The turbulent kinetic energy k (per unit mass) is [14]

$$k = \frac{1}{2}(\overline{u'u'} + \overline{v'v'} + \overline{w'w'}) \tag{3}$$

where $\overline{u'u'}$, $\overline{v'v'}$, and $\overline{w'w'}$ are the specific Reynolds normal stresses in the x, y, and z directions, respectively.

Velocity data were acquired with the measurement system in both its nominal position and rotated 90 deg, as shown in Fig. 6, to show that $\bar{w} = \bar{v}$ and $\overline{w'w'} = \overline{v'v'}$ at the inlet and that these values are much smaller than $\bar{u}$ and $\overline{u'u'}$. The measurements show that $\overline{v'v'} \approx \overline{w'w'} \neq \overline{u'u'}$, as shown in Fig. 7. The majority of the inlet plane has negligible fluctuations, but near the wall $\overline{u'u'} > \overline{v'v'} = \overline{w'w'}$ and $\overline{v'v'} = \overline{w'w'} < 0.1\ \mathrm{m^2/s^2}$. At this location, $\overline{u'u'} = 1.8 \pm 0.17\ \mathrm{m^2/s^2}$ justifying an approximation that $\overline{v'v'} = \overline{w'w'} \approx 0$. We note that this assumption does not hold true for the SRQ data farther downstream.

The turbulence dissipation rate ε is a function of the spatial derivatives of the fluctuating components of velocity and in tensor notation is

$$\varepsilon = \nu \overline{\frac{\partial u_i'}{\partial x_k} \frac{\partial u_i'}{\partial x_k}} \tag{4}$$

where repeated indices are summed. Not all of the components of the dissipation can be measured with the available diagnostics, but the largest of these components, $\overline{(\partial u'/\partial y)^2}$ can be computed from the instantaneous velocity field using the methods described in Ref. [20] to compute the derivatives. Using this conservative value for all of the derivative terms in the definition of ε and the measured kinematic viscosity, the inlet turbulence dissipation rate was found to be less than 10^{-4}. It is shown in the Appendix that RANS CFD models are insensitive to the inlet value of ε until several orders of magnitude larger than this value.

The inlet velocity is shown in the contour plot of Fig. 8. The inflow is mostly uniform except near the walls of the test section. Note that PIV measurements do not extend all the way to the wall in the z direction, as that measurement is impossible in orientation A. The plot shows the nine measured PIV planes mapped across the inlet. These data are provided to the numerical analyst as inflow data for the simulation. Any interpolation or wall treatments to make the inflow conditions closer to reality (such as applying a no-slip condition on all walls and defining the boundary layer near the $z = -150$ mm and 150 mm walls) are left to the analyst. One suggested method is to copy the unheated wall boundary layer to the other unheated walls and leave the heated wall as measured.

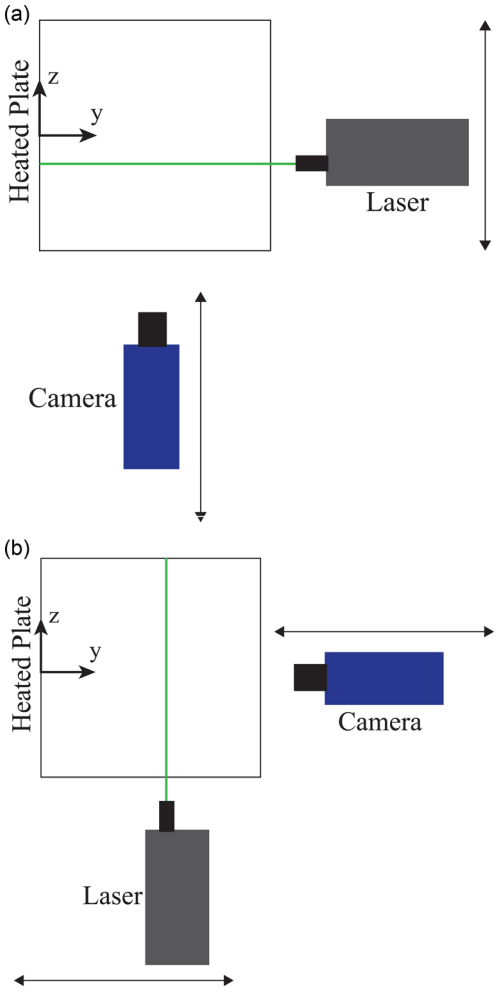

Fig. 6 The orientation of the camera and laser for PIV inflow data acquisition ($x = 0$). The laser and camera are traversed across the test section to obtain nine planes of velocity data. The flow direction is out of the page. (*a*) shows the nominal setup that is also used to obtain the velocity over the heat flux sensors and is referred to as orientation A. (*b*) shows the inlet profile specific orientation to obtain the *w* component of velocity and is orientation B.

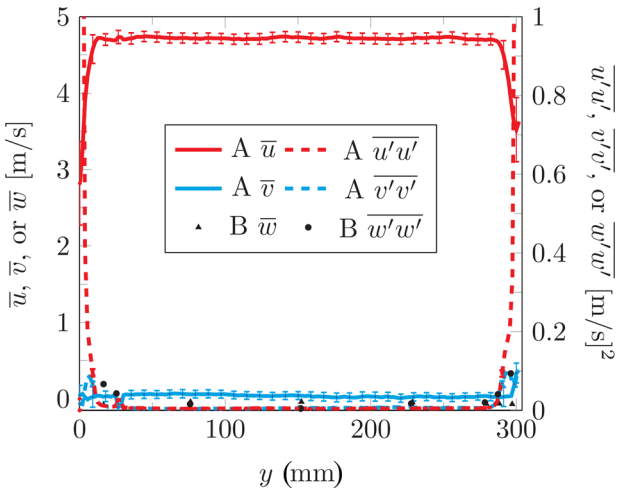

Fig. 7 The centerline inlet profiles for A and B orientations. The A orientation profiles are at $z = 0$. The points for the B orientation are data at the $z = 0$ intersections of profiles in the x–z plane. The uncertainty of the B orientation data is within the size of the symbols.

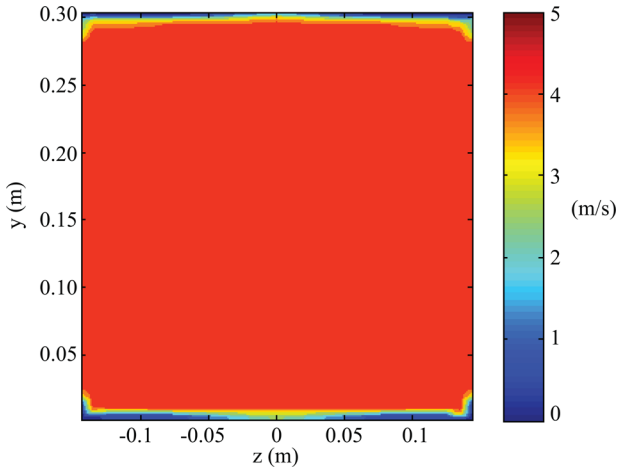

Fig. 8 A time-averaged streamwise velocity contour plot of the PIV measurements at the inlet of the test section, $x = 0$. This velocity field was formed by plotting nine vertical (constant z) profiles of velocity.

2.2 Instrumentation and Controls. A LABVIEW code was used to drive the acquisition of the temperature, heat flux, and room conditions and to control the room temperature, the plate temperature, the seeding for the PIV, and the blower speed. The National Instruments hardware included 5 NI-cDAQ-9188 chassis, which hold 20 NI-9213 16-channel thermocouple modules. All type K thermocouples were calibrated to a 0.3 °C source before installation. Another module and chassis controlled the larger voltage equipment, including the three power supplies for the six plate heaters and the room temperature control system. Figure 9 shows the test section assembly and the layout of the heaters and heat flux sensors. The room conditions were monitored and logged continuously, including temperature, pressure, and relative humidity. These were used to determine the air properties for each dataset.

Three heat flux sensors were embedded under the surface of the heated plate at positions P1 = 6.37 in. (162 mm), P2 = 30.62 in. (778 mm), and P3 = 54.87 in. (1394 mm) from the leading edge

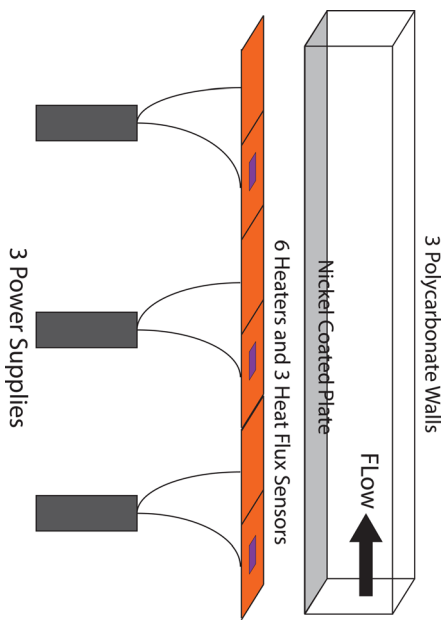

Fig. 9 A schematic showing the locations of heaters and heat flux sensors. Each of the three power supplies powers two heaters.

(see Fig. 9). These sensors were centered in the z direction. RdF Corporation heat flux sensors, model 20457-3, were used, with the first and third sensors having manufacturer-specified properties and an uncertainty of 5%. The second heat flux sensor had a larger uncertainty due to installation errors estimated to be 10% [21]. For additional details about the temperature, pressure, and velocity measurement sensors and systems, see Supplemental results which are available under "Supplemental Data 2" tab for this paper on the ASME Digital Collection.

To control the temperature of the heated plate, the thermocouples in the heat flux sensors were used as the inputs to a proportional-integral-derivative (PID) control system. A desired plate temperature was input, and the controller (with optimized gain and integral time of 0.5 and 2.5 mins, respectively) adjusted the voltage to the heaters. A nominally isothermal steady-state case was easily maintained to within the thermocouple accuracy of less than 1 °C over time. That is, the temperature control system maintained a steady state, even though the plate temperature was not perfectly isothermal.

To acquire the wall temperature BCs, all four walls were instrumented with thermocouples. The thermocouples in the heated plate were spaced at intervals of 2 in. (50.8 mm). The thermocouples in the two clear side walls were at $x = 0.0$, 33.66, 62.55, 96.84, 123.8, 166.4, and 192.4 cm and $y = 19.05$, 95.25, and 247.7 mm. On the top clear wall, the thermocouples were placed at $z = -76.2$, 0.0, and 76.2 mm and $x = 0.0$, 33.66, 76.2, 103.2, 137.5, 166.4, and 192.4 cm. The depth of the holes for placement of the thermocouples into the heated plate is included in the Supplemental results which are available under "Supplemental Data 2" tab for this paper on the ASME Digital Collection.

Pressure measurements were also acquired using a MKS 270D Baratron 1-Torr pressure sensor with a MKS 270D signal conditioner. Four pressure taps were installed in the wind tunnel at the contraction inlet, the contraction outlet, near the test section inlet, and the test section outlet.

Included with the BCs are the ambient air properties (atmospheric pressure, temperature, and relative humidity). The barometric pressure was acquired using an Apogee Instruments, Inc. SB-100. The temperature and humidity were acquired using a temperature/humidity probe (Omega HX93A).

The PIV camera was an Imager Intense 12-bit digital camera from LaVision [22]. The charge-coupled device sensor was 1376×1040 pixels with a pixel size of 6.45 μm (0.000254 in.) square. The laser pair was a New Wave Research Solo PIV III 15. Two lasers at 50 mJ/pulse and 532 nm could fire up to 15 Hz. Due to limitations of the camera, data could be acquired at 4 Hz in double-pulse mode.

The PIV data were acquired and processed using DaVis 8.1.6. A ruler was used to calibrate the camera for the inlet data, and a single plane calibration plate was used to scale and dewarp the images for the SRQ data using a pinhole model. The calibration plate used laser-etched circles on an anodized aluminum plate. The dots were 0.980 mm (0.039 in.) in diameter and spaced 3.175 mm (0.125 in.) apart.

The particle displacements were generally around 12 pixels in the free stream, with the particle diameters usually between 1 and 2 pixels. The small particle image diameters were unavoidable due to illumination issues for the large field of view at the inlet. The uncertainty method accounts for the variation in particle diameter and displacements, addressing any pixel locking errors. The images for the SRQ data used the entire imaging chip (1376×1040 pixels). The inlet data region of interest was generally 1376×256 pixels, capturing the inlet of the test section. The images were processed using the following steps after acquisition:

(1) The images were corrected for small vibrations and rotation based on the wall image. In particular, the wall image was forced to be vertical and in the same position for every image.
(2) The average image of the dataset was subtracted from the instantaneous images to decrease the background noise.

(3) Vectors were computed using 64×64 windows with one pass, then decreased to a 32×32 windows with 75% overlap for two passes. In addition, the SRQ images were processed with image correction, which is possible due to the two-dimensional, plate-based calibration.
(4) The PIV data were postprocessed with an allowable vector range of 0–10 m/s in $\bar{u}$ and −1 to 1 m/s in $\bar{v}$. The vectors were deleted if the correlation peak ratio was less than two. A median filter was used to remove vectors for which the difference to the average was greater than 1.75 × root mean square (RMS) of its neighbors and inserted (or reinserted) if the difference to the average was less than 2.5 × RMS of its neighbors. Also, groups with less than five vectors were removed and the allowable vector range was computed again.
(5) The time-average velocity and Reynolds stresses were also computed.

Two different lenses were used on the camera. A Nikon 105-mm lens and extension tube were used when acquiring images for the SRQ measurements over the heat flux sensors. A Nikon 28-mm lens was used when acquiring images for the inflow. In all cases, a 532 nm notch filter was placed over the lens to remove room light and decrease reflections (rhodamine paint was used on the highly reflective Teflon to shift reflected light outside the filter pass band).

The camera and laser were both mounted to Velmex [23] traverse stages that allow for synchronized motion in the y and z directions. The traverses were each independently controlled with LABVIEW. To move the equipment in the x direction, the hardware was designed to mount easily at increments of 5 in. (127 mm), with mounts for the laser and camera providing more accurate placement.

PIV measurements require seed particles distributed in the flow. Two Laskin nozzles were used to generate olive oil droplets that are approximately 0.8 μm in diameter. These devices are similar to those described by Kähler [24]. The droplets were then blown into a system of polyvinyl chloride pipe that is fixed to the inlet of the contraction of the wind tunnel (bottom of Fig. 4). The system was laid out in a grid pattern allowing for even dispersion of the seed particles. These pipes are upstream of the flow straighteners and screens and have no detectable impact on the test section inflow.

2.3 Measurement Uncertainties. The PIV uncertainty is determined using the methods described in Refs. [9,11,12]. The uncertainty of length dimensions comes from the resolution of the measurement devices and statistics of repeated measurements. These values are all included in the data in the Supplemental results which are available under "Supplemental Data" tab for this paper on the ASME Digital Collection. The remainder of this section will describe our estimate of uncertainties that are not as straight forward as those previously described.

2.3.1 Uncertainty of Friction Velocity. The friction velocity is found using two methods described below. The first directly calculates the wall shear using a linear fit to the data near the wall. The uncertainty of the wall shear velocity u_τ based on the velocity gradient at the wall is found using the Taylor series method [13] and the data reduction equation $u_\tau = \sqrt{\nu (du/dy)_w}$. The uncertainty of the shear velocity is

$$U_{u_\tau} = \sqrt{\left(U_{du/dy}\frac{\sqrt{\nu}}{2\sqrt{du/dy}}\right)^2 + \left(U_\nu \frac{\sqrt{du/dy}}{2\sqrt{\nu}}\right)^2} \tag{5}$$

where U_ν is the uncertainty of the kinematic viscosity

$$U_\nu = \sqrt{\left(U_\mu \frac{1}{\rho}\right)^2 + \left(U_\rho \frac{-\mu}{\rho^2}\right)^2} \tag{6}$$

and $U_{du/dy}$ is the uncertainty of the velocity gradient

$$U_{du/dy} = \sqrt{\left(\frac{U_{u1}}{dy}\right)^2 + \left(\frac{U_{u2}}{dy}\right)^2 + \left(U_{dy}\frac{u1-u2}{dy^2}\right)^2} \tag{7}$$

where the velocity uncertainties are computed using the methods described in Refs. [9–12] and the velocities are data points in the velocity profile. The dy term is the vector spacing of the data and the uncertainty of dy is explained below.

The dynamic viscosity μ is found from a polynomial fit to data contained in Ref. [25]. As a function of the temperature in Celsius, the viscosity is

$$\mu(T) = 1.714 \times 10^{-5} + 4.879 \times 10^{-8} T - 4.5675 \times 10^{-11} T^2 + 7.3469 \times 10^{-14} T^3 \tag{8}$$

The uncertainty of the viscosity is dominated by the uncertainty of the data in Ref. [25]. The density is found from the ideal gas law and the air density uncertainty is

$$U_\rho^2 = \left(\frac{U_P}{TR_{\text{air}}}\right)^2 + \left(U_T \frac{-PR_{\text{air}}}{(TR_{\text{air}})^2}\right)^2 + \left(U_{R_{\text{air}}}\frac{-PT}{(TR_{\text{air}})^2}\right)^2 \tag{9}$$

where the air gas constant is found from $R_{\text{air}} = 8.31434/M_{\text{mix}}$ and

$$M_{\text{mix}} = (1+\omega)\Big/\left(\frac{\omega}{18.02} + \frac{1}{28.97}\right) \tag{10}$$

The humidity ratio\ω is a function of the measured relative humidity, pressure, and temperature and is defined as

$$\omega = \frac{0.622}{\dfrac{P}{\phi P_{\text{sat}}} - 1} \tag{11}$$

with $P_{\text{sat}} = 0.57574 + 0.0554T + 4.1195 \times 10^{-4} T^2 + 6.0733 \times 10^{-5} T^3$. The uncertainty of the air gas constant is negligible. The uncertainty of this temperature is $U_T = 0.6\,^\circ$C (note that this is not a thermocouple, but a thermistor-based probe) and the uncertainty of the atmospheric pressure is $U_P = 1.5\%$ of reading.

2.3.2 Uncertainty of Wall Position. The most obvious method for setting the spatial origin in the velocity data is to locate an unmoving object (such as a wall) in the raw PIV images. However, the laser source commonly generates a wide flare in the camera image at the wall making it difficult to pinpoint its location. An example is shown in Fig. 10, which shows a small part of the image. The wall is the white band near the left side of the image.

This estimate can be improved upon using information from the turbulent flow along a wall. The error in the wall location was first

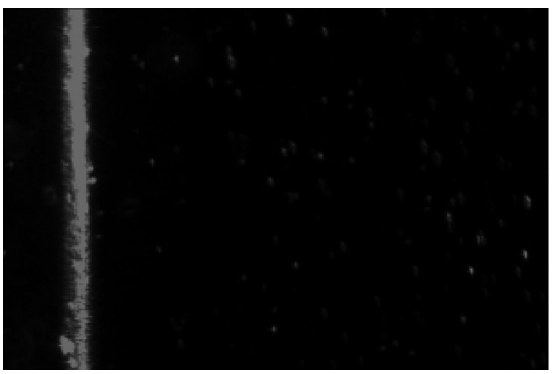

Fig. 10 An image of the wall, with the image width being 2.25 mm

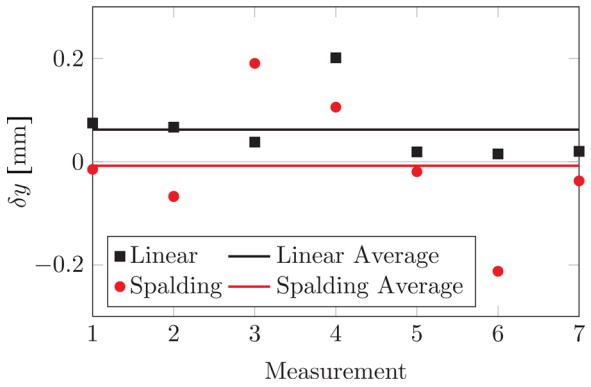

Fig. 11 The error of the wall location relative to the wall image using two methods. The scale factor is approximately 84 pixels/mm.

found by fitting theoretical (Spalding [26]) velocity profiles to the hundreds of streamwise time-averaged velocity data points (some of which are located in the viscous sublayer, and most of which are in the log-layer), and using the wall location as a parameter of the fit. The log-layer data have low uncertainty, but this procedure relies on the applicability of the Spalding model. Alternately, the wall location can be found by fitting a line through the three velocity values closest to the wall. These should behave linearly and go to zero at the wall. It was found that replications of this process, with the measurement system setup from scratch each time, resulted in large variations in the wall location error.

Seven replications are shown in Fig. 11. The error δy of each method relative to the wall location based on inspection of the raw images is shown. For both methods, the variations in the wall position error were on the order of 16 pixels. The average of these samples could be viewed as the bias of each method relative to the wall location by inspection. Unfortunately, we have no evidence that any one of these methods is clearly superior to any other, but these data are sufficient to provide a reasonable uncertainty estimate of the wall location. Based on the results, the Spalding fit method has very little bias and a 1-sigma random uncertainty of 0.13 mm.

3 Data Acquisition Procedures

For the inflow data, nine planes of two-component PIV data were acquired in orientation A shown in Fig. 6. The procedure for acquiring the inlet data is described as:

(1) Setup laser, camera, and traverse stages and align with the test section in space (the calibration target is fixed to the test section).
(2) Calibrate camera and match laser plane to calibration plane.
(3) Set acquisition timing for sufficient particle displacements, set seed flow rate, laser intensity, and f-stop (impacting particle image intensity and size).
(4) Stabilize room, wall, and flow conditions.
(5) Record PIV data, temperatures, heat flux, equipment position, blower speed, heater and seeding settings, camera and laser settings, and room conditions.
(6) Move to next plane and repeat the previous step.

The process for acquiring SRQ data is the same, except there is only one plane at which to acquire data ($z = 0$). The boundary layer flow images are acquired with the camera at a slight angle with respect to the plate to decrease the length of the light path through air, consisting of a density gradient that would otherwise distort the images. Because the angle is small, a planar scaling of the images was sufficient. The inlet data use 500 image pairs and the SRQ data use 1000 image pairs.

Table 1 The available data from the experiments described in this article. Corresponding uncertainties are included for each.

Buoyancy aided and opposed	
BCs	SRQs
Geometry	Heat flux (three locations)
Wall temperatures	Boundary layer velocity
Inlet temperature	Shear velocity
Inlet velocity	
Atmospheric conditions	

4 Validation Data Results

The following Secs. 4.2 and 4.3 describe measurements for isothermal forced convection for buoyancy-aided and buoyancy-opposed flow. The Reynolds number based on the test section hydraulic diameter and free stream velocity is 77,000. The data that are acquired and available to the reader are outlined in Table 1.

4.1 BCs. The geometry of the wind tunnel test section was measured prior to all experiments to provide the as-built (as opposed to as-designed) test section and is included in the Supplemental results which are available under "Supplemental Data 3" tab for this paper on the ASME Digital Collection with the measurement uncertainties outlined in the Supplemental results which are available under "Supplemental Data 4" tab for this paper on the ASME Digital Collection. The height and width of the test section were measured using a micrometer at the transparent-wall thermocouple locations, as described in the Supplemental results which are available under "Supplemental Data 2" tab for this paper on the ASME Digital Collection. The inflow velocity, inflow temperature, and wall temperature on all four walls were also recorded to provide the necessary BCs.

The average of all relevant cases is used as the BC. For example, there are 12 datasets for the forced convection isothermal case. The wall and inlet temperatures used for the BCs are the average of these 12 sets. The atmospheric conditions for the buoyancy-aided flow case including the measured barometric pressure, ambient temperature, and relative humidity are included in the Supplemental results which are available under "Supplemental Data 5" tab for this paper on the ASME Digital Collection. The atmospheric conditions for the buoyancy-opposed case are included in the Supplemental results which are available under "Supplemental Data 6" tab for this paper on the ASME Digital Collection.

4.2 Buoyancy-Aided Case. The first case presented is buoyancy-aided forced convection over a plate that was nominally isothermal and set to about 140 °C. The controller seeks isothermal heating, but the BC thermocouples are much more resolved spatially than the PID controller (which uses only three temperature readings as shown in Fig. 9), limiting the ability to actually reach isothermal heating. For example, the corner of the leading edge is 30 °C cooler than the maximum plate temperature.

The temperature BCs are included in the Supplemental results which are available under "Supplemental Data" tab for this paper on the ASME Digital Collection and there are five temperature files; four for walls and one for the inflow. Supplemental results which are available under "Supplemental Data 7" tab for this paper on the ASME Digital Collection contain the temperature of the heated wall ($y = 0$), Supplemental results which are available under "Supplemental Data 8" tab for this paper on the ASME Digital Collection contain the temperature of the top wall ($y = 12$ in.), Supplemental results which are available under "Supplemental Data 9" tab for this paper on the ASME Digital Collection contain the temperature of the left wall ($z = -6$ in.), Supplemental results which are available under "Supplemental Data 10" tab for this

Table 2 The "isothermal" heat flux results along with the Grashof to Reynolds number ratio (showing the cases are forced convection) and the momentum thickness Reynolds number

x position (mm)	Heat flux (W/m^2)	Re_x	$\mathrm{Gr}_x/\mathrm{Re}_x^2$	δ_2 (mm)	Re_{δ_2}
P1 = 162	1917	40,300	0.026	1.4	357
P2 = 778	1170	194,000	0.131	2.2	554
P3 = 1394	1356	347,000	0.232	2.3	564

paper on the ASME Digital Collection contain the temperature of the right wall ($z = 6$ in.), and Supplemental results which are available under "Supplemental Data 11" tab for this paper on the ASME Digital Collection contain the temperature of the inlet ($x = 0$ in.). The values are measured by the 312 thermocouples used in the experiment at the time the SRQ data were acquired. As there are 12 instances of SRQ and BC acquisitions for each case, these 12 BCs are averaged and the statistics are also reported in the csv files. The x, y, and z columns specify the position of each measurement in meters. The Temp column is temperature in Kelvin. The bias, precision, and total uncertainty of the temperature with 95% confidence are also presented.

The inlet velocity and inlet Reynolds stresses are included in the Supplemental results which are available under "Supplemental Data 12" tab for this paper on the ASME Digital Collection. The columns in data file are as follows: X, Y, and Z are positions of the vectors in meters. Columns u, v, and w are the velocities (m/s) in the x, y, and z directions, respectively. Columns $u'u'$, $v'v'$, $w'w'$, and $u'v'$ are the specific Reynolds stresses with the justified assumption that $\overline{v'v'} = \overline{w'w'}$. The uncertainty of the velocities is also included within the spreadsheet. Uu is the uncertainty of the $\bar{u}$ velocity, similarly with Uv and Uw for their respective velocity components. $Uuup$ is the upper uncertainty of $\overline{u'u'}$, and $Uuum$ is the lower uncertainty of $\overline{u'u'}$. The uncertainties of $\overline{v'v'}, \overline{u'v'}$, and $\overline{w'w'}$ are similarly notated.

The heat flux, Reynolds number, Richardson number, and momentum thickness Reynolds number are shown in Table 2 for three x locations. The flow at the location of the third heat flux sensor is near the boundary of the mixed convection ratio using the ratio specified in Ref. [14]. The momentum thickness Reynolds number was found at each heat flux sensor position. Kays and Crawford show that the critical momentum thickness Reynolds number is 162 [14].

Figure 12 shows the measured heat flux compared with two correlations. The measured heat flux is the heat flux reading from the sensors shown in Fig. 9 and is an ensemble average of the 12 acquisition cases for the buoyancy-aided forced isothermal condition. The trend labeled Kays is the heat flux predicted by the correlation [14]

$$\mathrm{St} = \frac{\mathrm{Nu}_x}{\mathrm{Re}_x \mathrm{Pr}} = \frac{0.0287\mathrm{Re}_x^{-0.2}}{0.169\mathrm{Re}_x^{-0.1}(13.2\mathrm{Pr} - 9.25) + 0.85} \tag{12}$$

The Incropera trend is based on the correlation for convection over an isothermal flat plate [27] and is

$$\mathrm{Nu}_x = 0.0296\mathrm{Re}_x^{4/5}\mathrm{Pr}^{1/3} \tag{13}$$

The Stanton number is the Nusselt number divided by the product of the Reynolds and Prandtl numbers. Once the Nusselt number is computed, the heat flux can be found as $q'' = \mathrm{Nu}_x k(T_x - T_\infty)/x$. Note that the correlation trends are not smooth, a result of the measured centerline plate temperature, which has small gradients.

The boundary layer streamwise velocity profiles in the wall-normal direction are shown in Fig. 13. Note that only the near wall region is shown, and the larger velocities at P1 do not correspond to a larger total flow rate compared to P2 and P3. The higher velocity at the first heat flux sensor is a repeatable trend

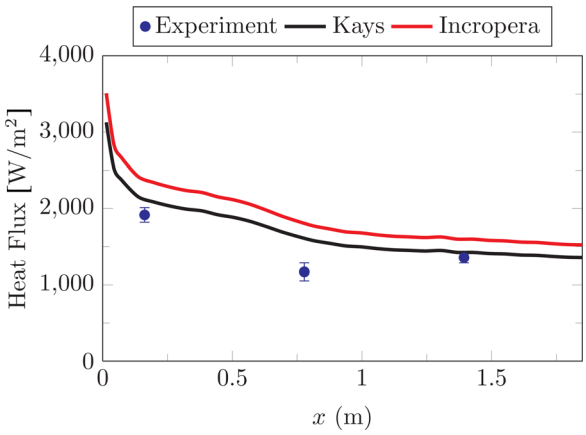

Fig. 12 The measured heat flux and two correlations with the Kays trend found from Eq. (12) and the Incropera from Eq. (13) for the buoyancy-aided case

and results from the thickening of the boundary layer between P1 and P2. These data are shown nondimensionally while dimensional plots are provided in the validation database included with this document.

In addition to the time-mean velocity, the specific Reynolds normal stress $\overline{u'u'}$ may also be used as a SRQ. The uncertainty bands on velocity and specific Reynolds stresses are at the 95% confidence level.

The cross-stream time-mean velocity $\bar{v}$, Reynolds normal stress $\overline{v'v'}$, and Reynolds shear stress $\overline{u'v'}$ cross-stream profiles are not shown here but are available in the Supplemental results which are available under "Supplemental Data" tab for this paper on the ASME Digital Collection. The magnitudes of these quantities are small compared to the velocity resolution of the PIV, and this is reflected in the uncertainty bands.

The wall coordinate quantities u_τ, κ, y_0, and B can be found using the method described by Kendall and Koochesfahani [26]. A curve fit to the Spalding profile yields shear velocities shown in Table 3, where the Spalding profile is

$$y^+ = u^+ + \exp(-\kappa B)\left[\exp(\kappa u^+) - 1 - \kappa u^+ - \frac{(\kappa u^+)^2}{2} - \frac{(\kappa u^+)^3}{6}\right] \tag{14}$$

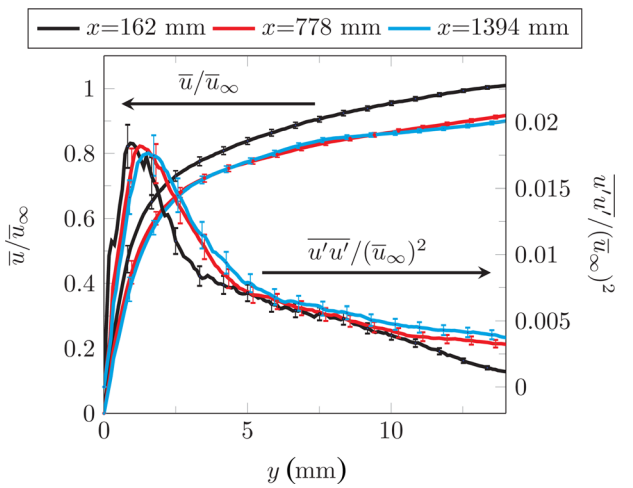

Fig. 13 The nondimensional boundary layer time-mean streamwise velocity and Reynolds normal stress for the flow over the three heat flux sensor positions with $\bar{u}_\infty = 4.49$ m/s for the buoyancy-aided case

Table 3 The von Kármán constant, *y*-intercept, shear velocity from the Spalding fit, and the shear velocity from a linear fit near the wall at the heat flux sensor positions for the buoyancy-aided case are tabulated

Position	κ	B	u_τ Spalding	u_τ linear
P1	0.41	5.00	0.248	0.233 ± 0.004
P1	0.36	5.49	0.228	
P2	0.41	5.00	0.233	0.216 ± 0.004
P2	0.405	5.61	0.223	
P3	0.41	5.00	0.235	0.216 ± 0.004
P3	0.354	4.85	0.219	

Units of u_τ are m/s.

and $y^+ = (y - y_0)u_\tau/\nu$ and $u^+ = \bar{u}_\infty/u_\tau$. Two results are shown for each profile: one with the traditional $\kappa = 0.41$ and $B = 5.0$ and a second where κ and B are found in the fitting process. Care was taken to exclude wake region data for the curve fit. Using the shear velocities shown in Table 3, the wall coordinate profiles for velocity at the heat flux sensor positions are shown in Fig. 14.

The data are acquired at the streamwise (x) location of the three heat flux sensors. Note that the v velocities are very small and near the velocity resolution of the PIV measurements (thus, the large uncertainty bands). The velocity profiles at the first, second, and third heat flux sensor positions are included in the Supplemental results which are available under "Supplemental Data 13" tab for this paper on the ASME Digital Collection containing the velocity data over the first heat flux sensor position, Supplemental results which are available under "Supplemental Data 14" tab for this paper on the ASME Digital Collection over the second, and Supplemental results which are available under "Supplemental Data 15" tab for this paper on the ASME Digital Collection over the third heat flux sensor position. The files contain columns of data as follows: Position x, y, z in meters, the time-average velocities in the streamwise and wall-normal directions in m/s, u and v respectively. The specific Reynolds stresses $\overline{u'u'}$, $\overline{v'v'}$, and $\overline{u'v'}$ are also included. The uncertainty of these values are given along with the upper (such as *Uuup*) and lower (such as *Uuum*) uncertainty components of the Reynolds stresses.

The shear velocity is also an SRQ and is presented in Table 3. The heat flux SRQ is contained in the Supplemental results which are available under "Supplemental Data 16" tab for this paper on the ASME Digital Collection. The columns in this file are the position, the heat flux, the bias uncertainty of the heat flux measurements, the precision uncertainty of the heat flux measurement, and the total uncertainty of the heat flux.

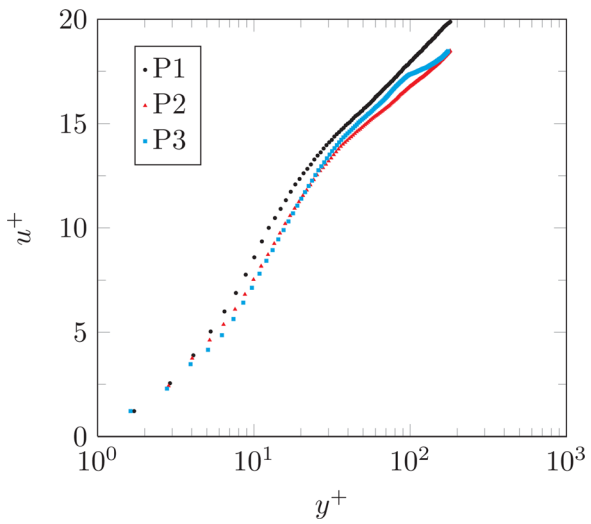

Fig. 14 The wall coordinate profiles at each heat flux sensor position using the variable κ and B for the buoyancy-aided case

Table 4 The buoyancy-opposed isothermal forced convection heat flux results along with the Grashof to Reynolds number ratio and the momentum thickness Reynolds number

x position (mm)	Heat flux (W/m^2)	Re_x	$\mathrm{Gr}_x/\mathrm{Re}_x^2$	δ_2 (mm)	Re_{δ_2}
P1 = 162	1947	41,400	0.02	1.8	466
P2 = 778	1241	199,000	0.12	2.8	713
P3 = 1394	1442	357,000	0.22	3.2	813

4.3 Buoyancy-Opposed Case. The same heating conditions and flow rate are considered with the wind tunnel rotated in such a way that the forced flow is downward, opposing the effects of buoyancy. The heated wall temperature BCs for the buoyancy-opposed case are included in the Supplemental results which are available under "Supplemental Data 17" tab for this paper on the ASME Digital Collection. The top wall ($y = 12$ in.) temperatures are in the Supplemental results which are available under "Supplemental Data 18" tab for this paper on the ASME Digital Collection. The left ($z = -6$ in.) wall temperatures are in the Supplemental results which are available under "Supplemental Data 19" tab for this paper on the ASME Digital Collection. The right ($z = 6$ in.) wall temperatures are in the Supplemental results which are available under "Supplemental Data 20" tab for this paper on the ASME Digital Collection. The inlet temperature is provided in the Supplemental results which are available under "Supplemental Data 21" tab for this paper on the ASME Digital Collection. The inlet flow field is provided in the Supplemental results which are available under "Supplemental Data 27" tab for this paper on the ASME Digital Collection. The file structure for the buoyancy-opposed case BCs is identical to the buoyancy-aided case in Sec. 4.2.

The heat flux, local Reynolds number, the ratio of the Grashof to Reynolds number squared, the momentum thickness, and momentum thickness Reynolds number are all tabulated in Table 4. It is noted that the values for the convection ratio are very similar to the buoyancy-aided case. The momentum thickness and momentum thickness Reynolds number show a different trend as a function of x position than the buoyancy-aided case. The buoyancy-aided case had very similar values at the second and third positions, whereas the buoyancy-opposed case shows an increase. This suggests that the two flows will show a different boundary layer development based solely on the influence of gravity.

The heat flux is plotted in Fig. 15 and compared with the two correlations presented previously. The subtle differences between these results and the SRQs presented in Fig. 12 are discussed further in Sec. 5.2.

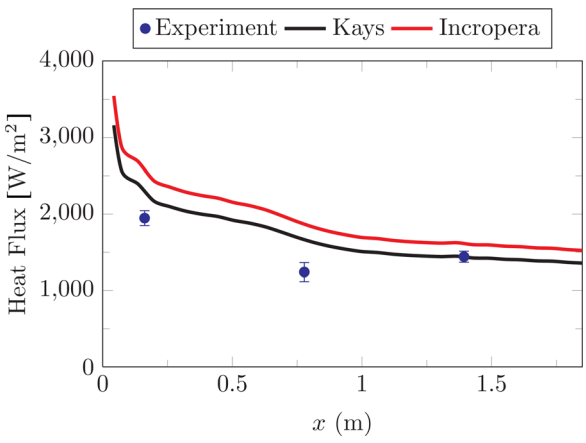

Fig. 15 The measured heat flux and two correlations with the Kays trend found from Eq. (12) and the Incropera trend from Eq. (13) for the buoyancy-opposed case

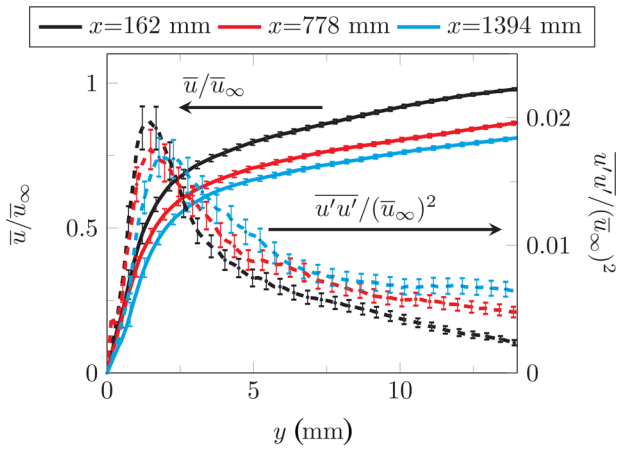

Fig. 16 The nondimensional boundary layer time-mean streamwise velocity and Reynolds normal stress for the flow over the three heat flux sensor positions with $\bar{u}_\infty = 4.56$ m/s for the buoyancy-opposed case

The boundary layer velocity profiles for the buoyancy-opposed isothermal forced convection case are plotted in Fig. 16. Note that the velocity profiles for the second and third positions are not as similar as they are in the buoyancy-aided case. This demonstrates that this forced convection flow has buoyancy effects and will be discussed more in Sec. 5.2.

The wall shear velocities computed using the two methods described above are tabulated in Table 5. Comparing the values in Table 5 to those in Table 3, the values at the first position are similar, but the second and third positions are not. The linear method shows a larger difference between the two cases than the Spalding fit method.

The SRQ data are included in the Supplemental results which are available under "Supplemental Data" tab for this paper on the ASME Digital Collection and the file structure is the same as the aided case, so the description is not replicated. The velocity profile over the first heat flux sensor is provided in the Supplemental results which are available under "Supplemental Data 22" tab for this paper on the ASME Digital Collection. The velocity over the second and third heat flux sensors is contained in the Supplemental results which are available under "Supplemental Data 23 and 24" tab for this paper on the ASME Digital Collection, respectively. The shear velocity is also an SRQ and is presented in Table 5. The heat flux SRQ is presented in the Supplemental results which are available under "Supplemental Data 25" tab for this paper on the ASME Digital Collection.

5 Discussion

5.1 Repeatability. In this section, the repeatability of the velocity measurement is considered, as suggested by Oberkampf and Trucano [28]. Figure 17 shows the boundary layer velocity for the several repeats of data at each position. Excellent repeatability is found in all cases. We note that these measurements were recorded several months apart, with a disassembly, reassembly, and recalibration of the PIV equipment between the second (r2) and third (r3) cases. A recalibration was performed between the first (r1) and second cases (r2). Note that a third measurement was not done for P2 and P3. Both the inlet and the boundary layer at the first position were found to be repeatable during the acquisition of the third measurement.

Figure 18 shows these profiles as a difference from the mean of the data of all replications at each of the locations P1, P2, and P3.

Table 5 The von Kármán constant, intercept, shear velocity from the Spalding fit, and the shear velocity from a linear fit near the wall at the heat flux sensor positions for the buoyancy-opposed isothermal forced convection case

Position	κ	B	u_τ Spalding	u_τ linear
P1	0.41	5.00	0.244	0.184±0.016
P1	0.39	5.17	0.237	
P2	0.41	5.00	0.220	0.176±0.015
P2	0.448	4.40	0.240	
P3	0.41	5.00	0.210	0.137±0.017
P3	0.499	6.16	0.221	

Note that $\kappa = 0.41$ and $B = 5.0$ are classical values not optimized in the fit.

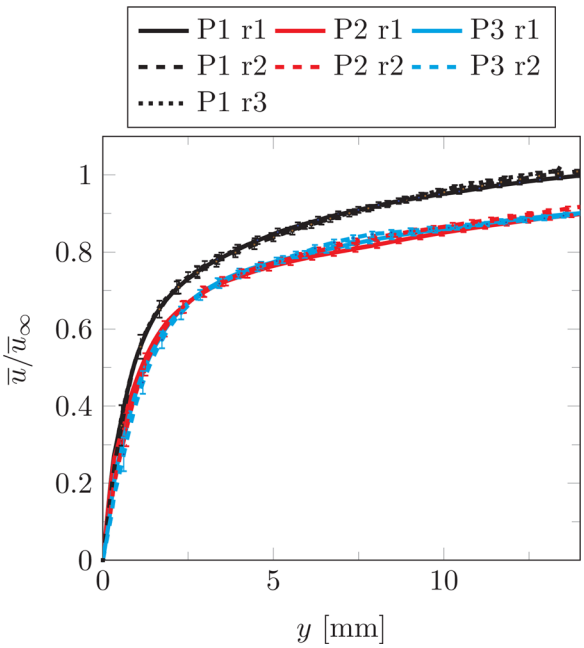

Fig. 17 The boundary layer streamwise velocity profiles for the flow over the three positions for three repeats of the isothermal measurement

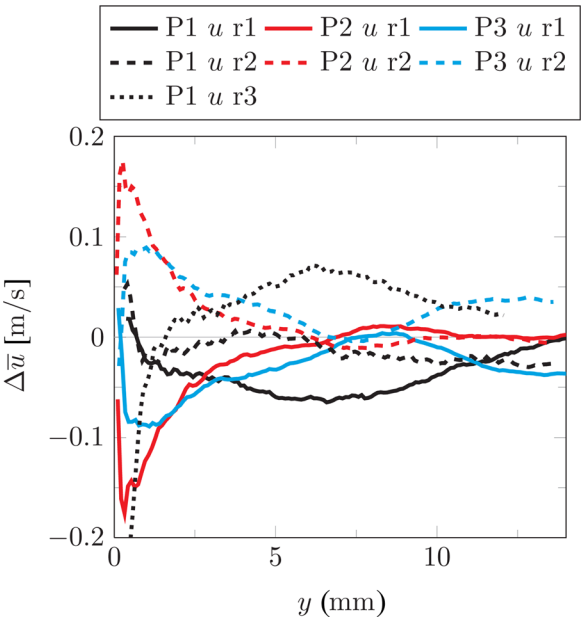

Fig. 18 The boundary layer streamwise velocity residuals for the flow over the three positions for three repeats of the isothermal measurement

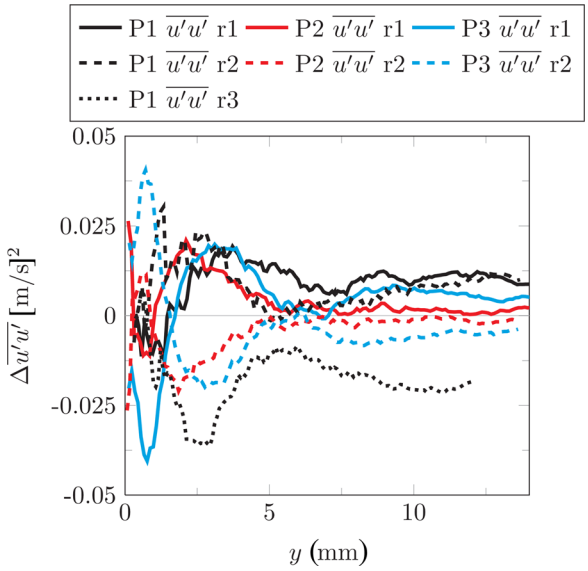

Fig. 19 The boundary layer streamwise velocity Reynolds normal stress residuals for the flow over the three positions for three repeats of the isothermal measurement

It is shown that three replications of the streamwise velocity over the first heat flux sensor have an average residual level of 0.05 with larger values near the wall. The PIV data near the wall have larger uncertainty. The large residual here could also result from an error in the y position in the presence of the large velocity gradient. The fact that the P2 and P3 trends are equal and opposite in Fig. 18 is because there are only two replications used to compute the average. The residuals for $\overline{u'u'}$, included in Fig. 19, are small.

5.2 Gravity Effects. Figure 20 shows the boundary layer velocity profiles for buoyancy aided and opposed isothermal forced convection. Gravity is seen to have an effect at P2 and P3. The relative difference (the difference between the buoyancy aided and opposed velocity divided by the buoyancy-opposed velocity, denoted $\delta\bar{u}_{F,G}$ where F means forced and G means gravity) for the isothermal forced convection is also shown in Fig. 20. The difference between the aided and opposed cases increases with streamwise length, suggesting that gravity affects the development of the boundary layer in these cases.

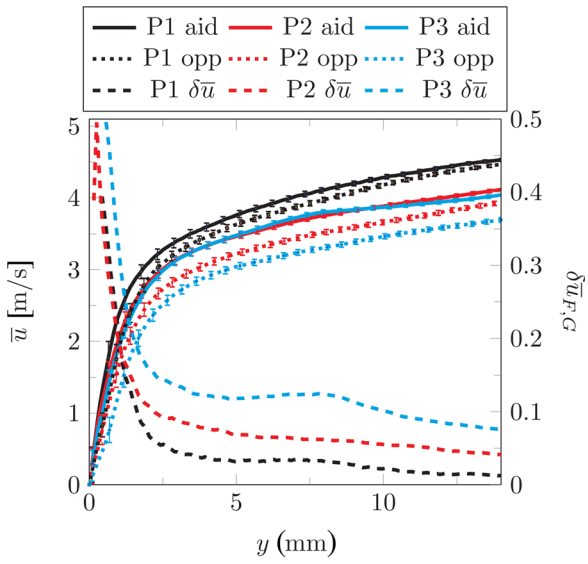

Fig. 20 The boundary layer velocity comparison for the isothermal forced convection buoyancy aided and opposed cases. The relative difference between the cases is also plotted as $\delta\bar{u}_{F,G}$.

5.3 Buoyancy Influence on Heat Flux. Now we consider the buoyancy influence on heat flux from the plate. Wang et al. showed data comparing the effects of buoyancy on heat transfer for buoyancy aided and opposed flow [17]. The Nusselt number is divided by a forced convection Nusselt number and plotted as a function of the special buoyancy parameter

$$\mathrm{Bo}^* = \frac{\mathrm{Gr}^*}{\mathrm{Re}^{3.425}\mathrm{Pr}^{0.8}} \tag{15}$$

This is shown in Fig. 21 and is compared with the data presented in Ref. [17].

In this analysis, the characteristic length of the Nusselt number Nu is the hydraulic diameter of the test section (12 in.). The developing, variable property forced convection Nusselt number Nu_f is

$$\mathrm{Nu}_f = C \times 0.0228\mathrm{Re}^{0.79}\mathrm{Pr}^{0.4}\left(\frac{T_s}{T_\infty}\right)^{-0.34} \tag{16}$$

with

$$C = 1.0 + \left(\frac{x}{D_h}\right)^{-0.29}\exp\left(-0.07\frac{x}{D_h}\right)\left[0.69 + \frac{5520}{\mathrm{Re}}\left(\frac{x}{D_h}\right)^{-0.7}\right] \tag{17}$$

as described in Ref. [17].

It is shown in the Wang et al. data and study [17] that the buoyancy-aided flow experiences a suppression of heat transfer followed by a recovery of the heat flux for an increase in buoyancy effects. The data obtained in the present study show a similar trend. For example, the buoyancy-aided case shows a decrease in the Nusselt number ratio from position 1 to 2 and an increase again from 2 to 3 (right to left in Fig. 21). The buoyancy-opposed forced case shows a suppression of heat flux similar to the buoyancy-aided case. The difference from unity at each position

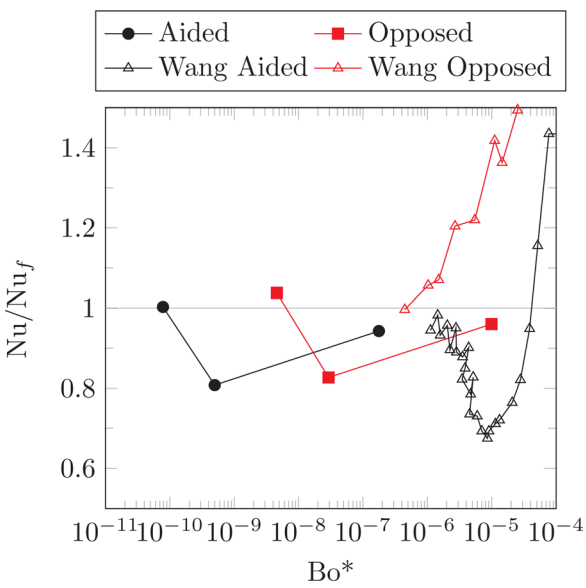

Fig. 21 A plot of the Nusselt number ratio versus the special buoyancy parameter for the data in this study and the data presented in Ref. [17]

is nearly the same for the two cases. The difference from unity at the third position for the buoyancy-aided case is negligible. However, for the buoyancy-opposed case, there is an improvement of heat transfer. This is due to the change in the direction of gravity.

5.4 Comparison of Classical Boundary Layer Shape Factors. The shape factor H, which is the ratio of the displacement thickness and the momentum thickness, is plotted in Fig. 22. The shape factor is plotted as a function of a second shape factor, η, which is defined as [29]

$$\eta = 1 - \left(\frac{\bar{u}(H)}{\bar{u}_\infty}\right)^2 \tag{18}$$

The $\bar{u}(H)$ term in Eq. (18) is the measured velocity at a distance H from the wall. The expected trend for η as a function of H is [29]

$$\eta_{\text{expected}} = 1 - \left[\frac{H-1}{H(H+1)}\right]^{H-1} \tag{19}$$

It is noted that for $\eta > 0.46$, a pressure rise exists in the flow [29]. From Fig. 22, we see that all of the buoyancy-aided cases are in the adverse pressure range. The experimental measurements also match trends shown in the data presented by Schlichting (see Fig. 22.6 in Ref. [29]). The text also states that separation occurs near $\eta \approx 0.8$. However, the data show no signs of separation.

To help understand if one should expect heating to impact the shape factor analysis, an unheated case is compared to a heated case. An additional two datasets that are not part of the validation dataset are now considered. They include an unheated and heated flow at a Reynolds number (based on hydraulic diameter) of 13,400. This flow is much slower than the cases considered previously, having a free stream velocity of 0.7 m/s. The buoyancy effects on the flow are significant for this flow rate. The velocity profiles for these additional cases are shown in Fig. 23. It is obvious that the heating accelerates the boundary layer when compared with the unheated case. In both cases, the Reynolds normal stress is small.

The corresponding shape factor correlation is included in Fig. 22 labeled as heated, unheated, and heated max velocity. Notice that when the free stream velocity is used to compute η in the heated case (solid square), the resultant point is far different

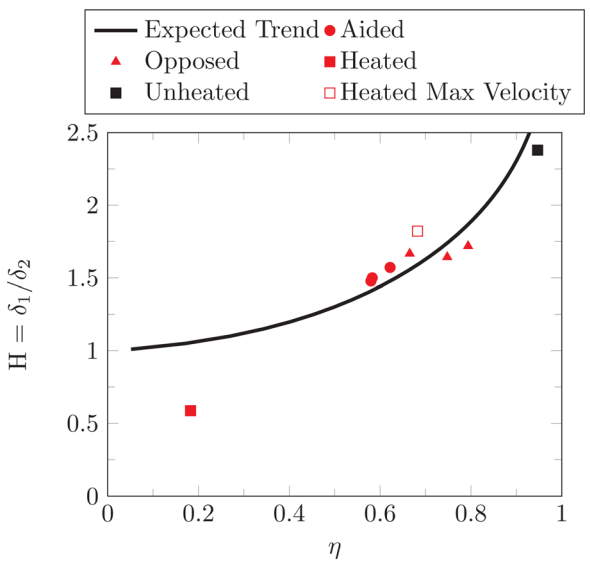

Fig. 22 A comparison of the classic shape factor with the expected trend as a function of the second shape factor η (see Eq. (18))

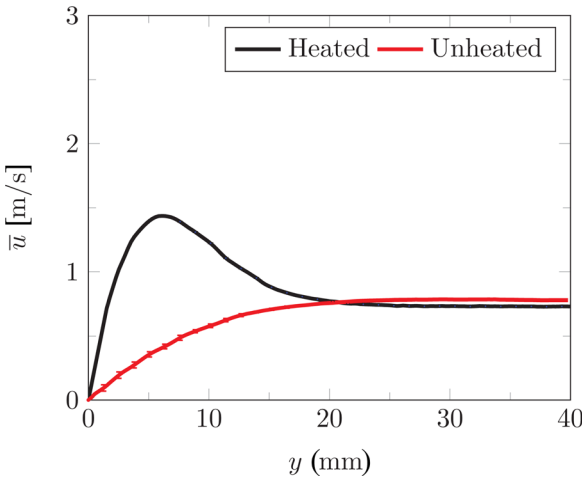

Fig. 23 The boundary layer velocity profiles for an unheated and heated low Reynolds number flow

from an expected trend. The free stream velocity is used in the literature and the other cases previously presented. However, if the maximum velocity is used (heated max velocity, hollow square), the point is closer to expected values. The unheated case is near the expected trend as well (solid square). This suggests that the boundary layers considered in this flow behave similarly to unheated boundary layers considered in the classical literature. Also, when discussing this shape factor trend, the maximum velocity should be used, particularly when significant accelerations are in the flow. The maximum velocity is higher than the free stream velocity for the low Reynolds number case shown by Fig. 23.

6 Conclusions

This work describes a CFD validation experiment for turbulent forced convection using guidelines described by Oberkampf and Roy [6] and Oberkampf and Smith [1]. It represents a departure from typical journal articles in that the aim of the study is not discovery, but rather to carefully measure all inputs and outputs of a CFD RANS simulation for the purpose of validation. A database in the Supplemental results which are available under "Supplemental Data" tab for this paper on the ASME Digital Collection is used to make the data (boundary and inflow conditions as well as system response) available digitally. This is the first in a series of convection validation data experiments that will be made available for CFD validation.

Acknowledgment

This research was funded by the DOE Office of Nuclear Energy's Nuclear Energy University Programs. The support of the Nuclear Regulatory Commission was also gratefully acknowledged. The authors also thank Professor Nam Dinh and Dr. William Oberkampf for their helpful discussions and insight.

Nomenclature

B = coefficient for wall coordinate profiles
dy = PIV data vector spacing
g = standard gravity constant
Gr_x = Grashof number
h = convection coefficient
H = boundary layer shape factor, δ_1/δ_2
k = turbulent kinetic energy
k_r = material property for radiation emission
n = index of refraction
Nu_x = Nusselt number

P = pressure
Pr = Prandtl number
Re_x = Reynolds number
Re_{δ_2} = momentum thickness Reynolds number
St_x = Stanton number
T = temperature
T_L = clear Lexan wall temperature
T_s = surface temperature
T_∞ = free stream temperature
$\bar{u}$ = mean streamwise velocity
$\bar{u}_\infty$ = free stream velocity
u_τ = shear velocity
$\overline{u'u'}$ = variance of u
$u1$ = velocity at a point in the profile
$u2$ = velocity at a second point in the profile
U_P = uncertainty of pressure
U_T = uncertainty of temperature
U_μ = uncertainty of dynamic viscosity
U_ν = uncertainty of kinematic viscosity
U_ρ = uncertainty of density
$U_{du/dy}$ = uncertainty of the velocity gradient
U_{u1} = uncertainty of velocity at a point
U_{u2} = uncertainty of velocity at a second point
U_{u_τ} = uncertainty of shear velocity
u' = instantaneous velocity fluctuation
$\bar{v}$ = mean velocity normal to wall
$\overline{v'v'}$ = variance of v
$\bar{w}$ = mean velocity normal to $\bar{u}$ and $\bar{v}$
$\overline{w'w'}$ = variance of w
x = direction parallel with flow
y = direction normal to plate
y_0 = correction for the wall location
z = direction normal to x and y plane (right-handed system)
β = the volumetric thermal expansion coefficient of air
δ_2 = the momentum thickness of the boundary layer
ε = turbulence dissipation rate
ε_L = emissivity of Lexan wall
ε_n = emissivity of nickel-coated plate
η = a secondary boundary layer shape factor
κ = von Kármán constant
μ = dynamic viscosity
ν = kinematic viscosity
ρ = fluid density
σ = Stefan–Boltzmann constant

Appendix: CFD Sensitivity to Inlet ε

The turbulence dissipation rate ε is a function of the spatial derivatives of the fluctuating components of velocity (cf. Eq. (4)). Since ε cannot be directly measured in this study, the sensitivity of a RANS model to inlet ε was investigated. Four simulations were run using several uniform distributions of ε at the inlet of the test section; $\varepsilon = 0$, 10^{-6}, 10^{-3}, and 10^{1}. For more information regarding the simulation parameters, see Ref. [21]. Additionally, a distribution of ε was found using the measured k and the common expression

$$\varepsilon = 0.09^{3/4}\frac{k^{3/2}}{l} \tag{20}$$

where l is 0.07 times the equivalent pipe diameter [30,31]. The equivalent pipe diameter can be computed from Heubscher's equation as [32]

$$d_{\mathrm{eq}} = 1.3\frac{(ab)^{0.625}}{(a+b)^{0.25}} \tag{21}$$

There is some controversy about this equation and there are several other suggestions for computing the equivalent pipe diameter. However, the differences result in similar values of ε.

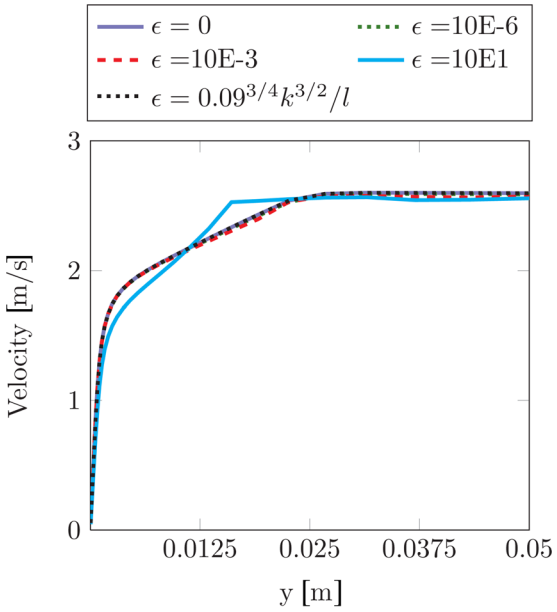

Fig. 24 The streamwise velocity at the first heat flux sensor position for several inlet ε treatments

Using these five profiles of ε, the effects on a velocity profile are shown in Fig. 24. Only the largest values of ε affect the simulation results. Using Eq. (20) at the inlet yields an inlet turbulence dissipation rate below 0.01. Profiles of other SRQs at the three heat flux sensor locations show the same trend as Fig. 24, with $\varepsilon = 10^1$ being the only case having significant influence on the SRQ. This insensitivity of CFD to ε was noted by Wilcox [31, p. 148] who states that investing resources into accurately finding ε is unwise.

References

[1] Oberkampf, W., and Smith, B., 2014, "Assessment Criteria for Computational Fluid Dynamics Validation Benchmark Experiments," AIAA SciTech Conference, AIAA, http://arc.aiaa.org/doi/abs/10.2514/6.2014-0205
[2] CFD-Online, 2013, "Validation Cases Links References," http://www.cfd-online.com/Links/refs.html
[3] NPARC Alliance, 2013, "Turbulent Flat Plate," http://www.grc.nasa.gov/WWW/wind/valid/fpturb/fpturb.html
[4] ERCoFTC, 2013, "Classic Collection Database," http://cfd.mace.manchester.ac.uk/ercoftac/classif.html
[5] Experimental Fluid Dynamics Laboratory, 2014, "Buoyancy Aided Forced Convection Database," http://efdl.neng.usu.edu/ValidationPages/FC_Validation/Main.html
[6] Oberkampf, W. L., and Roy, C. J., 2010, *Verification and Validation in Scientific Computing*, Cambridge University Press, New York.
[7] Oberkampf, W. L., Sindir, M., and Conlisk, A., 1998, *Guide for the Verification and Validation of Computational Fluid Dynamics Simulations*, American Institute of Aeronautics and Astronautics, Reston, VA.
[8] ASME, 2009, "Standard for Verification and Validation in Computational Fluid Dynamics and Heat Transfer," ASME Standard V&V 20-2009, New York.
[9] Timmins, B. H., Wilson, B. W., Smith, B. L., and Vlachos, P. P., 2012, "A Method for Automatic Estimation of Instantaneous Local Uncertainty in Particle Image Velocimetry Measurements," Exp. Fluids, **53**(4), pp. 1133–1147.
[10] Warner, S. O., and Smith, B. L., 2014, "Autocorrelation-Based Estimate of Particle Image Density for Diffraction Limited Particle Images," Meas. Sci. Technol. **25**(6).
[11] Wilson, B. M., and Smith, B. L., 2013, "Uncertainty on PIV Mean and Fluctuating Velocity Due to Bias and Random Errors," Meas. Sci. Technol., **24**(3), p. 035302.
[12] Wilson, B. M., and Smith, B. L., 2013, "Taylor-Series and Monte-Carlo-Method Uncertainty Estimation of the Width of a Probability Distribution Based on Varying Bias and Random Error," Meas. Sci. Technol., **24**(3), p. 035301.
[13] Coleman, H. W., and Steele, W. G., 2009, *Experimentation, Validation, and Uncertainty Analysis for Engineers*, 3rd ed., Wiley, Hoboken, NJ.
[14] Kays, W. M., Crawford, M. E., and Weigand, B., 2004, *Convective Heat and Mass Transfer*, 4th ed., McGraw-Hill, New York.

[15] Lloyd, J., and Sparrow, E., 1970, "Combined Forced and Free Convection Flow on Vertical Surfaces," Int. J. Heat Mass Transfer, **13**(2), pp. 434–438.
[16] Gryzagoridis, J., 1975, "Combined Free and Forced Convection From an Isothermal Vertical Plate," Int. J. Heat Mass Transfer, **18**(7), pp. 911–916.
[17] Wang, J., Li, J., and Jackson, J., 2004, "A Study of the Influence of Buoyancy on Turbulent Flow in a Vertical Plane Passage," Int. J. Heat Fluid Flow, **25**(3), pp. 420–430.
[18] Hattori, Y., Tsuji, T., Nagano, Y., and Tanaka, N., 2001, "Effects of Freestream on Turbulent Combined-Convection Boundary Layer Along a Vertical Heated Plate," Int. J. Heat Fluid Flow, **22**(3), pp. 315–322.
[19] Howell, J. R., Siegel, R., and Mengüç, M. P., 2011, *Thermal Radiation Heat Transfer*, CRC Press, Boca Raton.
[20] Karri, S., Charonko, J. J., and Vlachos, P. P., 2009, "Robust Wall Gradient Estimation Using Radial Basis Functions and Proper Orthogonal Decomposition (POD) for Particle Image Velocimetry (PIV) Measured Fields," Meas. Sci. Technol., **20**(4), p. 045401.
[21] Harris, J., 2014, "A CFD Validation Experiment for Forced and Mixed Convection on a Vertical Heated Plate," Ph.D. thesis, Utah State University, Logan, UT.
[22] LaVision, "DaVis® Version 8.1," Goettingen, Germany, http://www.lavision.de/en/techniques/piv.php
[23] Velmex, Inc., "Linear Motor-Driven Bi- and UniSlide Assemblies," http://www.velmex.com/index.asp
[24] Kähler, C., 2003, "General Design and Operating Rules for Seeding Atomisers," 5th International Symposium on Particle Image Velocimetry.
[25] Weast, R. C., Astle, M. J., and Beyer, W. H., 1988, *CRC Handbook of Chemistry and Physics*, Vol. 69, CRC Press, Boca Raton.
[26] Kendall, A., and Koochesfahani, M., 2008, "A Method for Estimating Wall Friction in Turbulent Wall-Bounded Flows," Exp. Fluids, **44**(5), pp. 773–780.
[27] Incropera, F. P., and DeWitt, D. P., 2002, *Introduction to Heat and Mass Transfer*, 5th ed., Wiley, New York.
[28] Oberkampf, W. L., and Trucano, T. G., 2002, "Verification and Validation in Computational Fluid Dynamics," Prog. Aerosp. Sci., **38**(3), pp. 209–272.
[29] Schlichting, H., 1968, *Boundary-Layer Theory*, McGraw-Hill, New York.
[30] Versteeg, H. K., and Malalaskekera, W., 2007, *An Introduction to Computational Fluid Dynamics: The Finite Volume Method*, Prentice Hall, New York.
[31] Wilcox, D., 2010, *Turbulence Modeling for CFD*, 3rd ed., Vol. 93, DCW Industries, La Cañada, CA.
[32] Huebscher, R. G., 1948, "Friction Equivalents for Round, Square and Rectangular Ducts," ASHVE Trans. (ASHRAE Trans.), **54**, pp. 101–144.